Kang *et al. Geosci. Lett. (2018) 5:22*
https://doi.org/10.1186/s40562-018-0124-9

Geoscience Letters

RESEARCH LETTER

Open Access

The partitioning of poleward energy transport response between the atmosphere and Ekman flux to prescribed surface forcing in a simplified GCM

Sarah M. Kang[1*], Yechul Shin[1] and Francis Codron[2]

Abstract

Recent studies have indicated that ocean circulation damps the atmospheric energy transport response to hemispherically differential energy perturbations, thereby muting the shifts of the Inter-Tropical Convergence Zone (ITCZ). Here, we focus on the potential role of Ekman heat transport in modulating this atmospheric response. An idealized representation of Ekman-driven heat transport (F_E) is included in an aquaplanet slab ocean coupled to a gray radiation atmospheric model. We first alter the strength of F_E in the control climate by tuning the gross stability of the Ekman layer S_E. For a wide range of F_E, the total poleward transport of energy remains nearly unchanged, but the ocean transports an increasing share for larger S_E. The control climate is then perturbed by adding surface cooling in the Southern Hemisphere and warming in the Northern Hemisphere. The Ekman coupling damps the atmospheric energy transport response, as in previous coupled model experiments with full ocean dynamics. The ratio of the changes in Ekman to atmospheric energy transport is determined by the ratio of the gross stability in the Ekman layer to the atmosphere in the control climate, and is insensitive to the amplitude and location of forcing. We find that an unrealistically large S_E is needed to reproduce the ratio of the changes in cross-equatorial oceanic to atmospheric energy transport in fully coupled models. The limited damping effect of Ekman transport highlights the need to examine the roles of deep circulation and subtropical gyres, as well as ocean heat uptake processes.

Keywords: Ekman coupling, Energy transport partitioning, Gross stability

Background

The Inter-Tropical Convergence Zone (ITCZ) is a meridionally narrow band of surface wind convergence and heavy precipitation located near the equator. The ITCZ shifts meridionally toward a warmed hemisphere, even for energy perturbations far from the tropics: in response to hemispherically differential energy perturbations, the Hadley circulation adjusts to transport energy in the direction of its upper branch toward the cooled hemisphere, while moisture is transported in the opposite direction by its lower branch. Thus, the ITCZ shift is proportional to changes in the cross-equatorial atmospheric energy transport (Broccoli et al. 2006; Kang et al. 2008, 2009; Seo et al. 2014; Schneider et al. 2014).

The energy transport load in the coupled system is shared by the atmosphere and the ocean; thus, fully coupled model experiments indicate that the ITCZ is relatively insensitive to extratropical energy perturbations (Deser et al. 2015; Tomas et al. 2016; Kay et al. 2016; Hawcroft et al. 2017; Xiang et al. 2018). Mechoso et al. (2016) suggest that anomalous cooling over the Southern Ocean can substantially shift the ITCZ northward in fully coupled models, depending on the capacity of a model to simulate the sensitivity of stratocumulus clouds to underlying sea surface temperatures (SSTs). Nevertheless, the ITCZ in fully coupled models is less sensitive to

*Correspondence: skang@unist.ac.kr
[1] School of Urban and Environmental Engineering, Ulsan National Institute of Science and Technology, Ulsan, Republic of Korea
Full list of author information is available at the end of the article

extratropical perturbations than that in slab ocean models with no ocean dynamics.

Several studies have attributed the damped ITCZ shifts in fully coupled models to the mechanical coupling via surface wind stress between the atmospheric Hadley circulation and the subtropical overturning cells in the ocean (Green and Marshall 2017; Schneider 2017; Kang et al. 2018). The resulting positive coupling of atmospheric and oceanic meridional energy transport ensures that the atmosphere and ocean split the cross-equatorial energy transport load, leading to a damped ITCZ response. Kang et al. (2018 hereafter KSX18) propose that a step toward resolving the issue is to develop a hierarchy of ocean models. As the simplest case, they examine the effect of meridional heat advection by surface Ekman flow in isolation. In this study, we go one step further by including the effect of the deep return flow, by implementing a representation of Ekman transport that was introduced in Codron (2012) in an aquaplanet slab ocean model. We use a gray radiation atmospheric model because our goal is to elucidate the purely dynamical response of a coupled system in which complications of water vapor or cloud radiative feedbacks are absent. The results from a more comprehensive atmospheric model will be discussed in a subsequent study. We demonstrate that the ratio of changes in ocean Ekman to atmospheric energy transport depends on the gross stability of the ocean in the control climate, which is a tunable parameter in our model.

Model description and experimental design

The atmospheric model is a simplified moist general circulation model with gray radiation in which radiative fluxes are a function of only temperature; thus, water vapor and other constituents do not affect radiative transfer (Frierson et al. 2006, 2007). The model uses a spectral dynamical core at T42 horizontal resolution and 25 vertical levels. Solar radiation is an analytical function of only latitude. There is no seasonal or diurnal cycle in the model. The atmospheric model setup is similar to that used in KSX18, except the insolation profile: the parameter that controls the meridional gradient of insolation Δ_s is set to 1.4 as in Frierson et al. (2006), whereas KSX18 uses Δ_s of 0.8 to mimic the mean SST profile in GFDL AM2 (Anderson et al. 2004) coupled to an aquaplanet slab ocean under the annual-mean insolation. The current setup produces a mean SST profile close to the AM2 under perpetual equinox conditions. All experiments are integrated for 20 years, with a spin-up period of 10 years.

The lower boundary is a 50-m aquaplanet slab ocean with no continents or lateral boundaries; hence, the SSTs evolve in response to the net surface energy fluxes and the implemented ocean heat transport. The control experiment (denoted CNT) is run with no prescribed heating or cooling in the slab ocean. In KSX18, we consider only the effect of meridional heat advection by surface Ekman flow. Here, the effect of deep return flow is additionally accounted for by the scheme developed by Codron (2012). The ocean heat transport is represented by the Ekman-driven heat fluxes, with the meridional Ekman mass transport (M_E) computed from the surface zonal wind stress τ_x:

$$M_E = \frac{-f\tau_x}{\varepsilon^2 + f^2}. \quad (1)$$

f is the Coriolis parameter and the factor ε is added because the Ekman balance breaks down near the equator, and it has a value of $1.0 \times 10^{-5}\mathrm{s}^{-1}$, which corresponds to the Coriolis parameter f at $\sim 4^\circ$ latitude. The surface Ekman transport M_E is directed poleward in the region of tropical easterlies, while it is directed equatorward in the region of midlatitude westerlies (dashed lines in Fig. 1a).

The mass transport by a deep return flow is assumed to be equal and opposite to that in the surface mixed layer M_E. Then, the heating induced by the total Ekman transport (denoted H_E) can be obtained by the convergence of the heat transports by the surface Ekman flow at the surface slab temperature T_s and by the deep return flow at a lower temperature T_d

$$H_E = -\frac{\partial}{a\cos\varphi\,\partial\varphi}\{CM_E(T_s - T_d)\cos\varphi\}, \quad (2)$$

where a is the Earth's radius, ϕ is latitude in radians, and the specific heat capacity of water C has a value of 4180 J kg^{-1} K^{-1}. For reference, this term is the last in Eq. (6) of Codron (2012). As shown in Fig. 1b, cooling is induced by a divergence of the surface Ekman flow in the deep tropics (i.e., $H_E < 0$), while warming is induced by a convergence in the subtropics to midlatitudes (i.e., $H_E > 0$), inferring that the model reproduces the effect of the wind-driven subtropical cells.

The magnitude of the heating induced by the Ekman transport H_E is proportional to $T_s - T_d$, which is equivalent to the gross stability of the ocean Ekman layer. The return flow temperature (T_d) is diagnosed from the surface temperature (T_s), following the 1.5-layer scheme in Codron (2012), as

$$T_d = \alpha T_s + (1-\alpha)T_f, \quad (3)$$

where T_f is the freezing temperature of seawater (=271.3 K). This formulation ensures that T_d remains below the surface temperature T_s and above the freezing temperature T_f. The difference between T_s and T_d

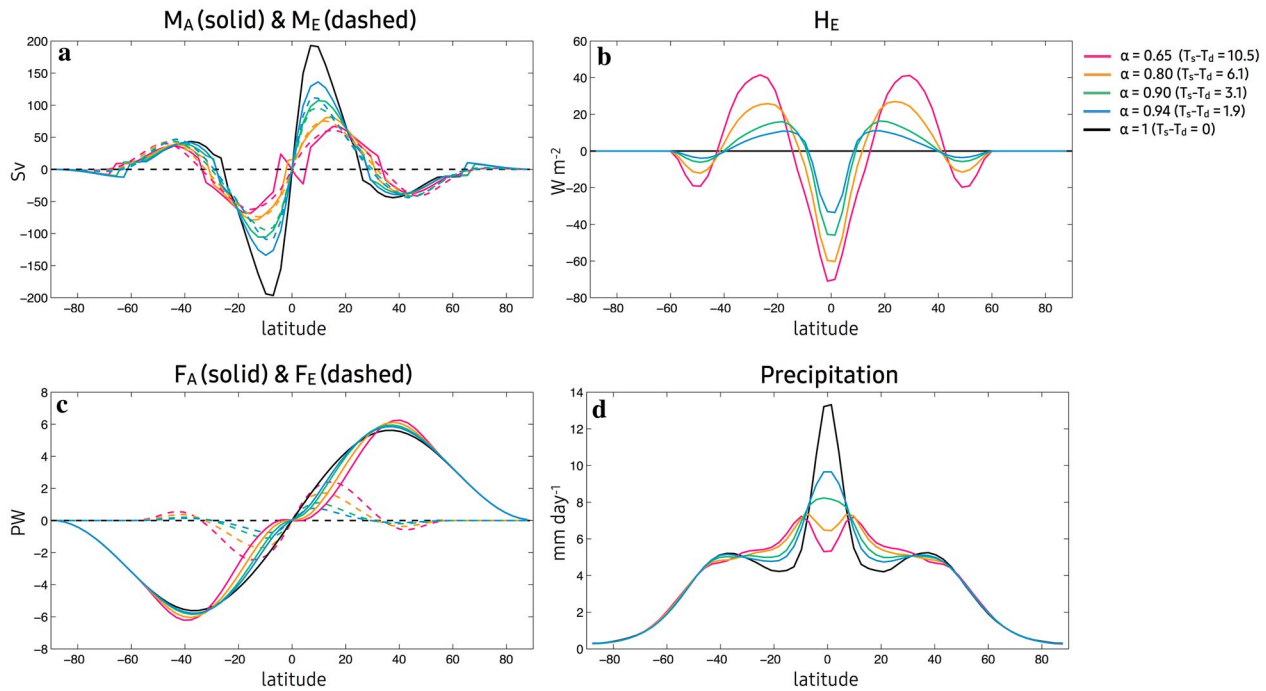

Fig. 1 The time- and zonal-mean state of CNT as a function of different $T_s - T_d$, obtained by varying α. **a** The mass transport by the atmospheric cells M_A (solid) and by the Ekman flow M_E (dashed) in Sv, **b** the heating induced by Ekman transport H_E in W m^{-2}, **c** the meridional energy transport by the atmosphere F_A (solid) and by the Ekman flow F_E (dashed) in PW, and **d** the precipitation in mm day^{-1}

becomes small at high latitudes (because T_s is close to T_f); thus, only a small amount of cooling is produced by the Ekman transport poleward of 40°S/N (Fig. 1b). The value of α determines the magnitude of the difference between T_s and T_d. We alter the α parameter from 0.65 to 0.94, which produces $T_s - T_d$ on the equator to be 10.45 K and 1.90 K, respectively. For simplicity, the notation $T_s - T_d$ will be used to refer to its equatorial value. Note that the model in KSX18 which only includes the meridional heat advection by surface Ekman flow can be regarded as the same model as in this study except $T_s - T_d$ being latitudinally constant.

In a series of sensitivity experiments, the CNT climate is perturbed by various forms of surface heating anomalies (denoted S), as illustrated in Additional file 1: Figure S1. We primarily discuss the experiments where surface heating ($S > 0$) is prescribed poleward of 40°N and compensating surface cooling ($S < 0$) is prescribed poleward of 40°S (Additional file 1: Figure S1a). A positive S can be described as the convergence of an implied ocean heat transport and vice versa, such that $S = -\frac{1}{2\pi a^2 \cos\varphi}\frac{\partial F_S}{\partial \varphi}$, where F_S is the implied ocean heat transport. Removing heat from the southern extratropics and adding it to the northern extratropics is equivalent to adding northward heat transport in the ocean across the equator (Additional file 1: Figure S1b). The amplitude of the prescribed surface heating is varied such that the cross-equatorial implied ocean heat transport F_{S0} ranges from 1.5 to 6.2 PW. Note that the high latitude forcing amplitude in a gray model must be four times as large as in a comprehensive model to produce a cross-equatorial atmospheric energy transport response of similar magnitude between the two models (Kang et al. 2009; Seo et al. 2014). For a reference case with $F_{S0} = 4.6$ PW, we examine the sensitivity to the gross stability of the ocean Ekman layer $T_s - T_d$ by varying α. We also examine the sensitivity to the latitudinal position of the forcing by prescribing surface heating anomalies at five different latitudinal bands with a latitudinal width of 16° (Additional file 1: Figure S1c). The center of the forced latitude band ϕ_0 ranges from 8° to 72°, and the maximum amplitude of the surface heating anomalies S is adjusted to ensure that the cross-equatorial transport F_{S0} is fixed at 1.5 PW (Additional file 1: Figure S1d). The experiments with varying F_{S0} and ϕ_0 are run with $\alpha = 0.70$ and 0.90, which, respectively, corresponds to $T_s - T_d = 9.04$ K and 3.11 K. The response to a prescribed surface heating anomaly is obtained by taking the difference between the climatology of the perturbed experiment and that of the control experiment with the same α.

Energy budget analysis

The atmospheric energy balance in a steady state in our model setup can be written as

$$R + H_E + S = \nabla \cdot F_A,$$

where R is the net downward top-of-atmosphere (TOA) radiative flux, H_E is the Ekman-induced heating computed by Eq. (2), S is the prescribed surface heating anomaly, and F_A is the atmospheric energy transport, which is the vertically integrated meridional moist static energy transport. The Ekman-induced heating H_E can be expressed as a convergence of the meridional heat transport by the Ekman flow (denoted F_E), so that $F_E(\varphi) = -\int_{-\frac{\pi}{2}}^{\varphi} \left(2\pi a^2 \cos\varphi H_E\right) d\varphi$. The unit for H_E is W m^{-2}, and the unit for F_E is W. The magnitude of the Ekman-induced heating is proportional to the gross stability of the Ekman layer (i.e., $T_s - T_d$), which is controlled by altering α in Eq. (3). There is no Ekman-driven heating (i.e., $H_E = 0$) when $\alpha = 1$. In our range of $T_s - T_d$, the cooling induced by the Ekman transport divergence H_E at the equator lies between 33 and 70 W m^{-2} (Fig. 1b), corresponding to the maximum meridional Ekman heat transport F_E between 0.76 and 2.40 PW, respectively (dashed lines in Fig. 1c). The cases with $T_s - T_d$ between 3.11 and 6.10 K can be regarded as realistic states (refer to Figs. 1c and 2a), considering that the observed estimate of ocean heat uptake is 48 W m^{-2} near the equator (Schneider 2017), while the observed estimate of the total meridional ocean heat transport reaches 1.7 ± 0.3 PW in the Northern Hemisphere and 1.2 ± 0.5 PW in the Southern Hemisphere (Trenberth and Fasullo 2008).

The difference in the atmospheric energy balance between the perturbed and control experiments can be written as (after expressing H_E and S as the convergence of the corresponding meridional transports)

$$\delta R - \nabla \cdot \delta F_E - \nabla \cdot \delta F_A = \nabla \cdot F_S,$$

where δ denotes the response to a prescribed surface heating anomaly S and $\nabla\cdot$ indicates $\frac{1}{2\pi a^2 \cos\varphi} \frac{\partial}{\partial \varphi}$. In the control experiment (CNT), $F_S = 0$ at all latitudes. The equation states that a prescribed forcing S is compensated by a three-way balance among the radiative fluxes and the meridional heat transport by the atmosphere and the Ekman flow. In the model without Ekman transport, the atmosphere is the only medium that transports energy; in which case, δF_A compensates the equatorial F_S by ~29% when the forcing S is prescribed in the extratropics while the rest is compensated locally by radiative fluxes. Ekman coupling is expected to reduce the burden on atmospheric energy transport. Then, the question arises as to what determines the partitioning of the energy transport response between the atmosphere and ocean Ekman flow.

Energy transport partitioning between the atmosphere and Ekman flow

Control climate

Figure 1 compares the time-mean states of CNTs with varying α. A decrease in α (or an increase in $T_s - T_d$) results in a greater energy transport by the Ekman flux (i.e., larger F_E), which then leads to a reduction in atmospheric energy transport (i.e., smaller F_A), as shown in Fig. 1c. The increase in F_E is compensated by the decrease in F_A, so that the total transport remains nearly constant with $T_s - T_d$ (Fig. 2a). A smaller F_A is accomplished by a weakening of the Hadley circulation mass transport M_A (solid lines in Fig. 1a). As a result, the tropical easterlies become weaker, which then induces a weaker Ekman mass transport M_E (dashed lines in Fig. 1a). This reduction in both M_A and M_E with $T_s - T_d$ can be clearly seen in Fig. 2b. The weaker M_A with larger $T_s - T_d$ also causes less moisture convergence in the equatorial region, which leads to a flatter ITCZ (Fig. 1d). For a sufficiently large $T_s - T_d$, the equatorial cooling induced by the Ekman flux becomes so strong (Fig. 1b) that the mean meridional atmospheric circulation descends in the equatorial region (Fig. 1a) to form a strong double ITCZ (Fig. 1d).

The mean overturning atmospheric mass transport M_A is computed as the peak of the mean meridional streamfunction in the midtroposphere at each latitude. Figures 1a and 2b suggest that the peak atmospheric mass transport is generally in the Ekman balance with the surface winds; that is, $M_A \approx M_E$. The mass and energy transports are related by the gross stability of a given fluid (Held 2001), which is measured as the energy contrast between the upper and lower branches. The gross stability of the ocean Ekman layer is $C(T_s - T_d)$, which is altered via the α parameter. We can also deduce the gross stability using

$$S_A = \frac{F_A}{M_A} \text{ and } S_E = \frac{F_E}{M_E}, \tag{4}$$

where S_A and S_E represent the gross stability of the atmosphere and ocean Ekman layer, respectively. Figure 2c compares S_A and S_E at 10° latitude in CNT as a function of $T_s - T_d$ (or α). As we discuss later, there is ambiguity in the treatment of M_E near the equator; thus, 10° latitude is used to represent the tropics. Note that we prefer to discuss in terms of $T_s - T_d$ rather than α, because it is more physically based and α is directly related to $T_s - T_d$ via Eq. (3). With increasing $T_s - T_d$,

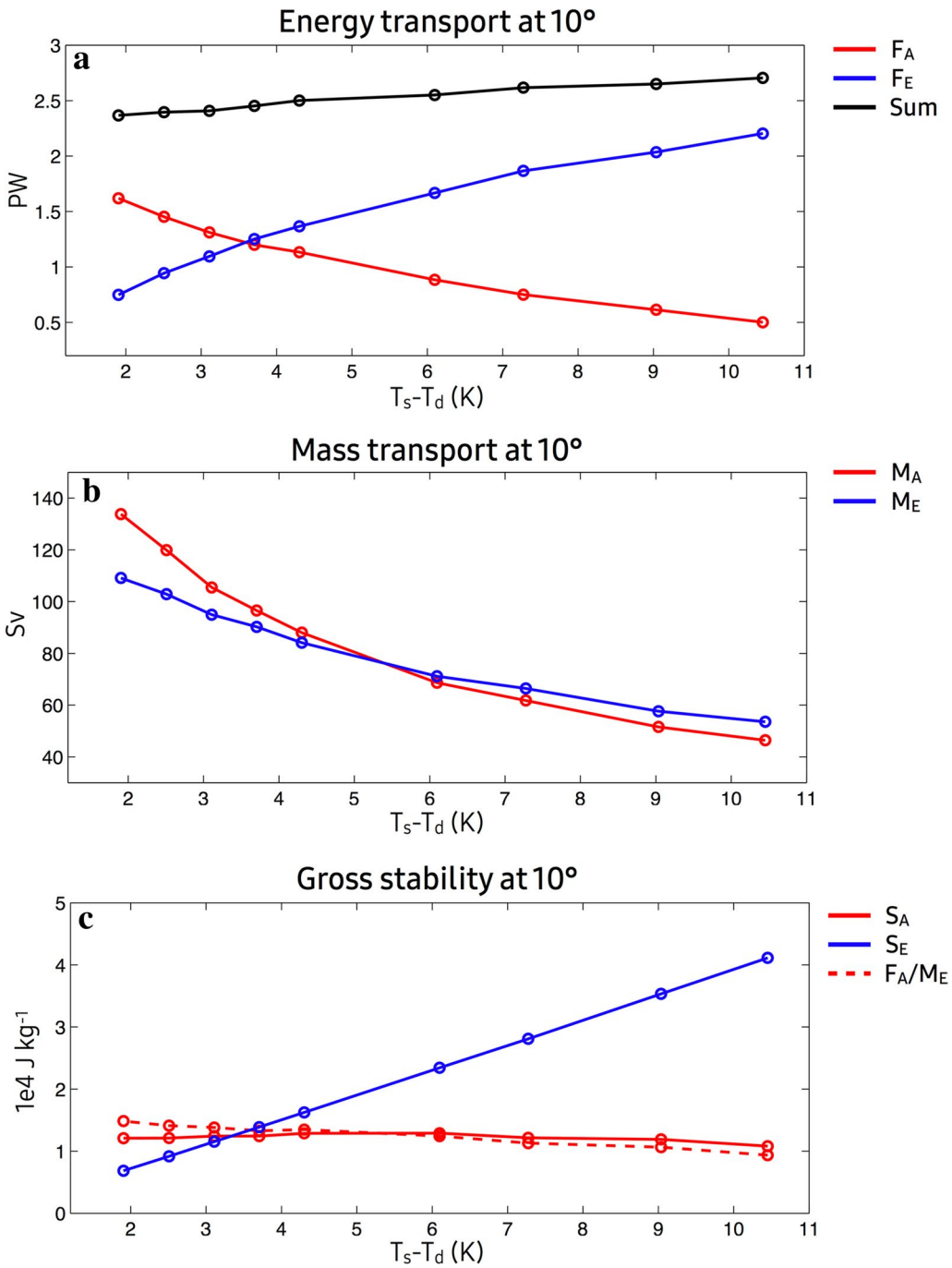

Fig. 2 **a** The meridional energy transport by the atmosphere F_A (red), the Ekman flow F_E (blue), and the sum (black) in PW, **b** the meridional mass transport by the atmosphere M_A (red) and the Ekman flow M_E (blue) in Sv, and **c** the gross stability of the atmosphere $S_A = F_A/M_A$ (red), its approximate estimate F_A/M_E (red dashed), and that of the Ekman flow $S_E = F_E/M_E$ (blue) in 10^4 J kg^{-1}, as a function of $T_s - T_d$ in CNT. All estimates are computed as the average of the absolute values at 10°S and 10°N

S_E increases linearly, whereas S_A remains constant. For $T_s - T_d > 4.30$ K, the gross stability of the Ekman layer S_E exceeds that of the atmosphere S_A, which results in more of the energy transported by the Ekman layer than transported by the atmosphere; that is, $F_E > F_A$ (Fig. 2a). An estimate of the gross stability of the atmosphere assuming $M_A = M_E$ (dashed red line in Fig. 2c) closely follows

the actual S_A (solid red line) due to the similarity between M_A and M_E (Fig. 2b).

Response to surface heating anomalies

Figure 3a compares the energy transport anomalies by the atmosphere δF_A and Ekman layer δF_E in response to the prescribed extratropical surface heating anomalies with $F_{S0} = 4.6$ PW (Additional file 1: Figure S1a). Shown in Fig. 3 are the average values between 10°S and 10°N as a function of $T_s - T_d$. The prescribed northward heat transport F_S is compensated by the anomalous southward energy transport by both the atmosphere and Ekman flow (i.e., $\delta F_A < 0$ and $\delta F_E < 0$). The response is linear to the forcing amplitude F_{S0} (not shown). The Ekman transport becomes more effective at compensating the prescribed forcing with increasing $T_s - T_d$, whereas less energy is compensated by the atmospheric transport.

We first discuss how the Ekman layer responds to compensate for the prescribed forcing. The prescribed northward heat transport F_S strengthens the southern Hadley circulation and weakens the northern Hadley circulation (so that more energy is transported southward to compensate for F_S). Then, the easterlies in the southern tropics strengthen, while the easterlies in the northern tropics weaken (Fig. 4a). These changes induce a southward Ekman mass transport response throughout the tropics (Fig. 4b). The anomalous Ekman mass transport exhibits a dip at the equator, with $\delta M_E \approx 0$, because M_E in both the perturbed and control experiments approaches zero near the equator following Eq. (1). The latitudinal pattern of δM_E closely determines that of δF_E (dashed in Fig. 4c). A convergence of δF_E warms the region between 40°S and 5°S ($\delta H_E > 0$) and a divergence of δF_E cools the region between 5°N and 40°N ($\delta H_E < 0$), as shown in Fig. 4d. This tropics–midlatitude component of the Ekman heat transport response partially compensates for the prescribed forcing that cools the Southern Hemisphere and warms the Northern Hemisphere, hence acting as a negative feedback. In the equatorial region, δF_E diverges south of the equator and converges north of the

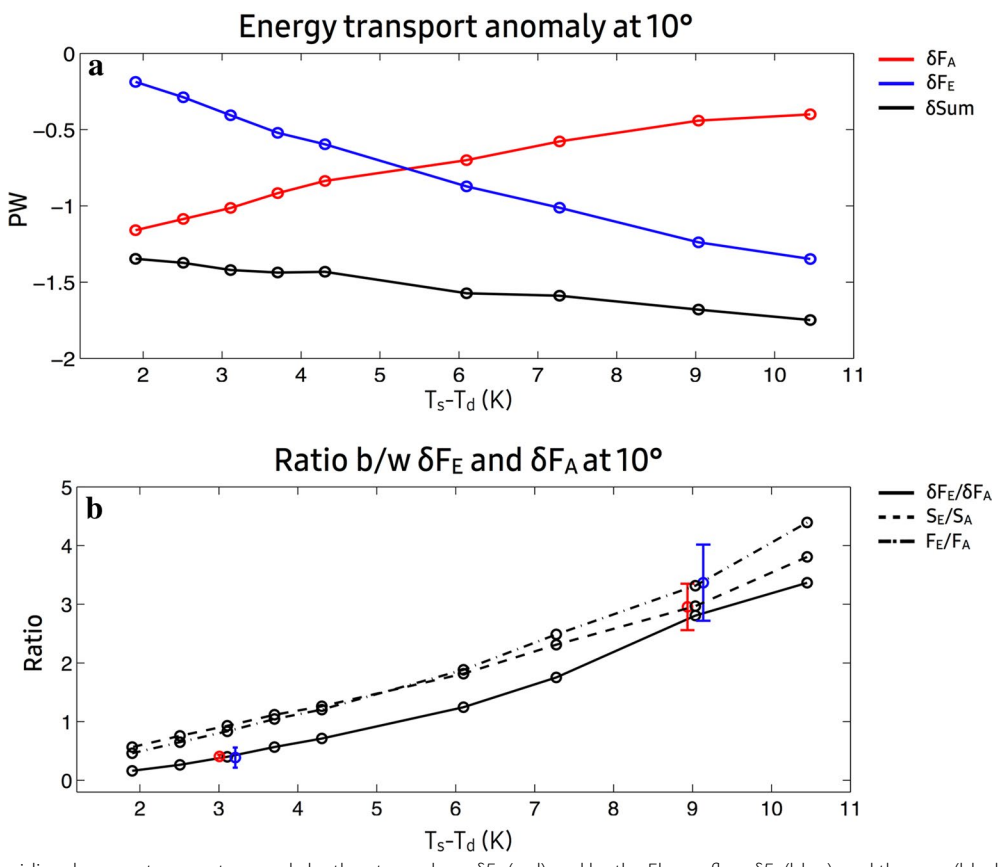

Fig. 3 **a** The meridional energy transport anomaly by the atmosphere δF_A (red) and by the Ekman flow δF_E (blue), and the sum (black) in PW, and **b** the ratio of the changes in Ekman to atmospheric energy transport $\delta F_E/\delta F_A$ (black solid), the ratio of Ekman to atmospheric gross stability in CNT S_E/S_A (black dashed), and the ratio of Ekman to atmospheric meridional energy transport in CNT F_E/F_A (black dash-dot), as a function of $T_s - T_d$. Red corresponds to the experiments with varying forcing amplitudes F_{S0} and blue to those with varying forced latitude bands φ_0. All estimates are the average anomalies at 10°S and 10°N

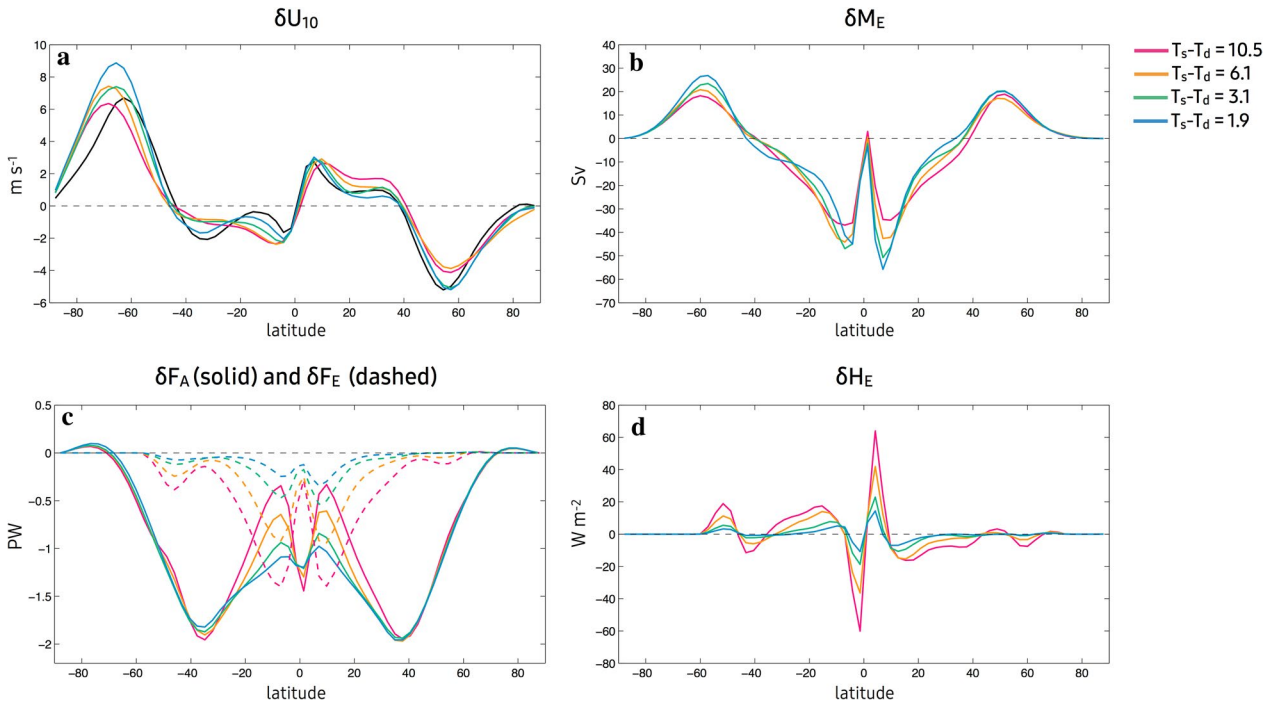

Fig. 4 Zonal-mean changes in **a** the zonal wind at 10 m in m s^{-1}, **b** the meridional Ekman mass transport δM_E in Sv, **c** the meridional energy transport by the atmosphere δF_A (solid) and by the Ekman flow δF_E (dashed) in PW, and **d** the Ekman-induced heating δH_E in W m^{-2} (solid) in the experiments with extratropical perturbations with $F_{S0} = 4.6$ PW

equator (Fig. 4c), which induces cooling and warming, respectively (Fig. 4d). This equatorial component of the Ekman heat transport response amplifies the prescribed forcing, hence acting as a local positive feedback. Poleward of 40°S/N, the anomalous Ekman mass transport which arises because of the extratropical jet shift is inefficient at producing anomalous heating because of the low $T_s - T_d$ value in the extratropics.

In the deep tropics, the Ekman transport has limited ability to compensate for the forcing (Fig. 4c). This is because of the equatorial positive feedback, which is expected to some degree in association with strengthened equatorial upwelling in the cooled hemisphere and weakened equatorial upwelling in the warmed hemisphere. Green and Marshall (2017) indeed note that the upwelling branch of the subtropical cells remains at the equator in response to hemispherically differential energy perturbations, while there is some strengthening in the cooled hemisphere and some weakening in the warmed hemisphere (see their Fig. 8). However, the equatorial positive feedback in Green and Marshall (2017) is weak; so, their ocean energy transport response does not exhibit as sharp of an equatorial dip. In our model setup, δM_E is constrained to zero at the equator following Eq. (1), which leads to $\delta F_E \approx 0$ regardless of $T_s - T_d$ (Fig. 4c). However, there is ambiguity in the treatment of equatorial flow, which affects the strength of equatorial positive feedback. In cases where M_E is assumed to be proportional to meridional winds near the equator, as in Codron (2012), δM_E should become positive at the equator, which would result in an even stronger equatorial positive feedback than that observed in our case. Instead, the near-equatorial flow can be treated to follow the local Sverdrup balance such that $M_E = -\partial_y \tau_x / \beta$, where $\beta = \mathrm{d}f/\mathrm{d}\phi$, in which case δM_E would be negative at the equator and would lead to a weaker equatorial positive feedback than that observed in our case (or even a negative one as in the rest of the tropics). Because of this ambiguity, we discuss the effect of Ekman modulation in the off-equatorial region at 10°S/N.

Figure 3b shows the ratio of Ekman to atmospheric energy transport response at 10° as a function of $T_s - T_d$. This ratio increases with $T_s - T_d$, and the anomalous Ekman energy transport begins to dominate over the anomalous atmospheric energy transport when $T_s - T_d = 5.2$ K. The fractional change in gross stability between the CNT and perturbed experiments is much smaller than that in mass transport for both the atmosphere and Ekman layer, so that $\delta F_A \approx S_A \delta M_A$ and $\delta F_E \approx S_E \delta M_E$ where S_A and S_E indicate the respective

CNT estimates for the different values of $T_s - T_d$. Further assuming $\delta M_A \approx \delta M_E$ and using $M_A \approx M_E$ in CNT (as confirmed in Fig. 2b) yields

$$\frac{\delta F_E}{\delta F_A} \approx \frac{S_E}{S_A} \approx \frac{F_E}{F_A}. \quad (5)$$

Equation (5) tells that the ratio $\delta F_E/\delta F_A$ can be predicted from the CNT experiment. That is, the increase in $\delta F_E/\delta F_A$ with $T_s - T_d$ is due to the increase in gross stability of the Ekman layer in CNT. Considering the simplicity of the theory, this prediction works well despite an overall slight overestimation (Fig. 3b). Figure 3b also shows the actual ratios in the experiments where either the forcing amplitude F_{S0} (red bars) or the forced latitude band ϕ_0 (blue bars) is varied, which are run with two different values of α, corresponding to $T_s - T_d = 3.11$ K and 9.04 K. The circle indicates the mean, and the bar indicates one standard deviation. One can find that the ratio $\delta F_E/\delta F_A$ is nearly insensitive to F_{S0} and ϕ_0, confirming that the ratio depends solely on $T_s - T_d$ or the gross stability of the Ekman layer in CNT.

A larger $\delta F_E/\delta F_A$, and thus a smaller δF_A, is expected to lead to a smaller shift in the tropical precipitation. The zonal-mean profile of the tropical precipitation response (Additional file 1: Figure S2) closely follows that of the Ekman heating response δH_E (Fig. 4d). The precipitation response between 10°S/N and 30°S/N becomes smaller for a larger $T_s - T_d$ due to stronger subtropical negative feedback. Hence, the centroid of zonal-mean precipitation between 20°S and 20°N (or 30°S–30°N) decreases with $T_s - T_d$ (Additional file 1: Figure S3), as would be expected. However, the precipitation response equatorward of 10° becomes larger with $T_s - T_d$ (Additional file 1: Figure S2) due to stronger equatorial positive feedback; thus, the centroid of zonal-mean precipitation between 10°S and 10°N increases with $T_s - T_d$ (Additional file 1: Figure S3). It is worth noting that the equatorial positive feedback is responsible for the large sensitivity of the precipitation centroid metric to the latitudinal range where it is computed.

Summary and discussion

Previous studies that neglected ocean dynamics suggested a strong influence of hemispherically differential thermal forcing at high latitudes on the tropical precipitation distribution. However, fully coupled model experiments indicate that this tropical precipitation response is muted as a larger fraction of the forcing is compensated by ocean energy transport rather than atmospheric energy transport in the tropics. To better understand the mechanism behind the extratropics–tropics teleconnection, we examine what controls the partitioning of energy transport between the atmosphere and ocean. In particular, we consider the effect of Ekman transport in isolation by including an idealized representation of Ekman-driven heat transport in an aquaplanet slab ocean coupled to a gray radiation atmospheric model.

Coupling of the Hadley circulation and the Ekman transport by the surface wind stress reduces the need for atmospheric energy transport. We show that the reduction depends on the gross stability of the Ekman layer, by utilizing a set of experiments where the difference between the surface temperature and the return flow temperature ($T_s - T_d$) is altered. For a larger $T_s - T_d$, there is a larger damping in the atmospheric energy transport response, or equivalently $\delta F_E/\delta F_A$ increases. The ratio of Ekman to atmospheric energy transport response $\delta F_E/\delta F_A$ is well predicted as the ratio between the gross stability of the Ekman layer and that of the atmosphere in the control experiment. Hence, the ratio is insensitive to the forcing profile, such as the forcing amplitude or the forced latitude band. However, the ratio $\delta F_E/\delta F_A$ greatly depends on the forcing amplitude in KSX18 where the effect of meridional Ekman heat advection by the surface flow is considered in isolation. The ratio in KSX18 varies between 0.43 and 2.33 in the equatorial region as the forcing amplitude F_{S0} varies from 5.8 to 1.1 PW, respectively. A reduction in the ratio with the forcing amplitude arises because of a stronger positive extratropical feedback associated with a larger jet shift. However, the extratropical positive feedback vanishes in our model because $T_s - T_d$ becomes negligible near 50°S/N, which is consistent with the low stratification of the ocean at these latitudes.

Fully coupled model experiments show a wide range in the ratio of the changes in cross-equatorial oceanic to atmospheric energy transport for extratropical energy perturbations (Deser et al. 2015; Tomas et al. 2016; Kay et al. 2016; Hawcroft et al. 2017; Mechoso et al. 2016; Xiang et al. 2018). The lower end of the ratio is approximately 1.5, while some models even indicate that the cross-equatorial energy transport response is entirely accomplished by the ocean. Although the wide spread should partly stem from differences in the details of the experimental setup, this study suggests that the model spread in the ocean stratification in the control climate may also contribute by modulating the efficiency of the Ekman compensation. However, it is difficult to directly compare the gray radiation model and more comprehensive models because cloud radiative effects may change the picture.

A cleaner comparison can be made with Green and Marshall (2017), which employs a gray radiation atmospheric model coupled to a full ocean model. The ratio of

cross-equatorial energy transport by the ocean to that by the atmosphere is 1.98 in their model. In our experiments, we consider the control climate with $T_s - T_d$ between 3.11 and 6.10 K is similar to the current Earth's climate, as discussed in "Energy budget analysis" section. Within that range of $T_s - T_d$, the ratio of Ekman to atmospheric energy transport response $\delta F_E/\delta F_A$ lies between 0.57 and 1.55, which is smaller than that in Green and Marshall (2017). One can also compute an observed estimate of $\delta F_E/\delta F_A$ based on Eq. (5). The Ekman energy transport F_E is computed by taking the zonal wind stress from the NCEP/NCAR reanalysis for 1979–2009 (Kalnay et al. 1996) with an assumption of 50 m mixed layer depth and $\alpha = 0.7$ that corresponds to $T_s - T_d = 9$ K, and the atmospheric energy transport F_A is taken from Donohoe et al. (2014) where the same reanalysis is used (Additional file 1: Figure S4). The reanalysis exhibits the ratio F_E/F_A of 0.95 at 10°S and 0.77 at 10°N, which is within the realistic range in our simple model. Our results indicate that Ekman transport alone cannot produce cross-equatorial energy transport as efficient as full ocean circulation. Factors such as deep ocean circulation and subtropical gyres other than Ekman transport should play a role in boosting oceanic compensation.

Additional file

Additional file 1: Figure S1. The prescribed surface heating (S; left column) and associated implied ocean heat transport (F_S; right column) in the experiments with varying (a, b) forcing amplitude F_{S0} and (c, d) forced latitude band φ_0. **Figure S2.** The zonal-mean response of precipitation in mm day^{-1} in the experiments with extratropical perturbations with F_{S0}=4.6 PW. **Figure S3.** The precipitation centroid of zonal-mean precipitation between 10°S and 10°N (red), 20°S and 20°N (green), and 30°S and 30°N (blue) as a function of $T_s - T_d$ in the experiments with extratropical perturbations with F_{S0} =4.6 PW. **Figure S4.** Atmospheric energy transport F_A (red) and Ekman energy transport F_E (blue) in the annual and zonal mean for 1979–2009. The atmospheric energy transport is from NCEP/NCAR reanalysis (Donohoe et al. 2014). The Ekman energy transport is computed by taking the zonal wind stress from NCEP/NCAR reanalysis with an assumption of 50 m mixed layer depth and $\alpha = 0.7$ that corresponds to $T_s - T_d = 9$K.

Abbreviations
ITCZ: Inter-Tropical Convergence Zone; SST: sea surface temperature.

Authors' contributions
SMK and FC designed the project. FC provided the 1.5-layer ocean model. YS performed the model experiments. SMK and YS analyzed the data. SMK led the writing of the manuscript. All authors read and approved the final manuscript.

Author details
[1] School of Urban and Environmental Engineering, Ulsan National Institute of Science and Technology, Ulsan, Republic of Korea. [2] Laboratoire d'Océanographie et du Climat (LOCEAN/IPSL), Sorbonne-Université, Paris, France.

Acknowledgements
The authors thank Shang-Ping Xie and Ken Takahashi for the helpful discussions during the early stage of work.

Competing interests
The authors declare that they have no competing interests.

Availability of data and materials
The dataset supporting the conclusions of this article is available in the PANGEA repository in https://doi.pangaea.de/10.1594/PANGAEA.886149.

Consent for publication
Not applicable.

Ethics approval and consent to participate
Not applicable.

Funding
S.M.K. and Y.S. were supported by the Basic Science Research Program through the National Research Foundation of Korea (NRF) funded by the Ministry of Science, ICT and Future Planning (2016R1A1A3A04005520). F.C. was supported by the French National Research Agency (ANR) project MORDICUS (ANR-13-SENV-0002).

Publisher's Note

Received: 1 February 2018 Accepted: 3 September 2018
Published online: 11 September 2018

References
Broccoli AJ, Dahl KA, Stouffer RJ (2006) Response of the ITCZ to Northern Hemisphere cooling. Geophys Res Lett. https://doi.org/10.1029/2005GL024546

Codron F (2012) Ekman heat transport for slab oceans. Clim Dyn 38(1–2):379–389

Deser C, Tomas RA, Sun L (2015) The role of ocean–atmosphere coupling in the zonal-mean atmospheric response to Arctic sea ice loss. J Clim 28(6):2168–2186

Donohoe A, Marshall J, Ferreira D, Armour K, McGee D (2014) The interannual variability of tropical precipitation and interhemispheric energy transport. J Clim 27:3377–3392

Frierson DM, Held IM, Zurita-Gotor P (2006) A gray-radiation aquaplanet moist GCM. Part I: static stability and eddy scale. J Atmos Sci 63(10):2548–2566

Frierson DM, Held IM, Zurita-Gotor P (2007) A gray-radiation aquaplanet moist GCM. Part II: energy transports in altered climates. J Atmos Sci 64(5):1680–1693

GFDL Global Atmospheric Model Development Team, Anderson JL, Balaji V, Broccoli AJ, Cooke WF, Delworth TL, Garner ST (2004) The new GFDL global atmosphere and land model AM2–LM2: Evaluation with prescribed SST simulations. J Clim 17(24):4641–4673

Green B, Marshall J (2017) Coupling of trade winds with ocean circulation damps ITCZ shifts. J Clim 30(12):4395–4411

Hawcroft M, Haywood JM, Collins M, Jones A, Jones AC, Stephens G (2017) Southern Ocean albedo, inter-hemispheric energy transports and the double ITCZ: global impacts of biases in a coupled model. Clim Dyn 48(7–8):2279–2295

Held IM (2001) The partitioning of the poleward energy transport between the tropical ocean and atmosphere. J Atmos Sci 58:943–948. https://doi.org/10.1175/1520-0469(2001)058%3c0943:TPOTPE%3e2.0.CO;2

Kalnay E et al (1996) The NCEP/NCAR 40-year reanalysis project. Bull Am Meteorol Soc 77:437–471. https://doi.org/10.1175/1520-0477(1996)077,0437:TNYRP.2.0.CO;2

Kang SM, Held IM, Frierson DM, Zhao M (2008) The response of the ITCZ to extratropical thermal forcing: idealized slab-ocean experiments with a GCM. J Clim 21(14):3521–3532

Kang SM, Frierson DM, Held IM (2009) The tropical response to extratropical thermal forcing in an idealized GCM: the importance of radiative feedbacks and convective parameterization. J Atmos Sci 66(9):2812–2827
Kang SM, Shin Y, Xie SP (2018) Extratropical forcing and tropical rainfall distribution: energetics framework and ocean Ekman advection. npj Climate and Atmospheric. Science 1(1):2
Kay JE, Wall C, Yettella V, Medeiros B, Hannay C, Caldwell P, Bitz C (2016) Global climate impacts of fixing the Southern Ocean shortwave radiation bias in the Community Earth System Model (CESM). J Clim 29(12):4617–4636
Mechoso CR, Losada T, Koseki S, Mohino-Harris E, Keenlyside N, Castaño-Tierno A, Myers TA, Rodrigues-Fonseca B, Toniazzo T (2016) Can reducing the incoming energy flux over the Southern Ocean in a CGCM improve its simulation of tropical climate? Geophys Res Lett 43(20):11057–11063
Schneider T (2017) Feedback of atmosphere-ocean coupling on shifts of the intertropical convergence zone. Geophys Res Lett 44(22):11644–11653
Schneider T, Bischoff T, Haug GH (2014) Migrations and dynamics of the intertropical convergence zone. Nature 513(7516):45
Seo J, Kang SM, Frierson DM (2014) Sensitivity of intertropical convergence zone movement to the latitudinal position of thermal forcing. J Clim 27(8):3035–3042
Tomas RA, Deser C, Sun L (2016) The role of ocean heat transport in the global climate response to projected Arctic sea ice loss. J Clim 29(19):6841–6859
Trenberth KE, Fasullo JT (2008) An observational estimate of inferred ocean energy divergence. J Phys Oceanogr 38(5):984–999
Xiang B, Zhao M, Ming Y, Yu W, Kang SM (2018) Contrasting impacts of radiative forcing in the southern ocean versus southern tropics on ITCZ position and energy transport in one GFDL climate model. J Clim 31:5609–5628